Title

Experimental and Computational Evaluation of a Sodium-Rich Anti-Perovskite for Solid State Electrolytes

Journal

Journal of The Electrochemical Society, 163(10)

ISSN

0013-4651

Authors

Nguyen, Han
Hy, Sunny
Wu, Erik
et al.

Publication Date

2016

DOI

10.1149/2.0091610jes

Peer reviewed

Journal of The Electrochemical Society, **163** (10) A2165-A2171 (2016)
0013-4651/2016/163(10)/A2165/7/$33.00 © The Electrochemical Society

Experimental and Computational Evaluation of a Sodium-Rich Anti-Perovskite for Solid State Electrolytes

Han Nguyen,[*] Sunny Hy, Erik Wu,[*] Zhi Deng, Mojtaba Samiee, Thomas Yersak, Jian Luo,[**] Shyue Ping Ong,[**] and Ying Shirley Meng[,z]**

Department of NanoEngineering, University of California San Diego, La Jolla, California 92093-0448, USA

In this study we experimentally investigated the effects of two processing techniques on the sodium-rich anti-perovskite, Na_3OBr; namely, conventional cold pressing (CP) and spark plasma sintering (SPS). We demonstrated that the electrolyte can be synthesized via a single-step solid state reaction. We compared the CP and SPS processed samples using XRD, SEM, and EIS. From these analyses it was found that SPS reduced Na_3OBr's interfacial impedance by three orders of magnitude, which translated into an increase in the overall ionic conductivity and a reduction in the activation energy, from 1.142 eV to 0.837 eV. DFT was used to probe the mechanisms for ionic transport in Na-rich Na_3OBr. The formation energies of ion diffusion-facilitating defects in Na_3OBr were found to be much higher compared to the lithium-rich anti-perovskites (LiRAP), which can explain the difference in overall ionic conductivity between the two.

Manuscript submitted May 24, 2016; revised manuscript received July 19, 2016. Published August 4, 2016.

Batteries with liquid electrolytes are ubiquitous since they are economical and practical. They can be found in consumer electronics, power tools, electric vehicles, and many other electronic devices that we encounter in our everyday lives. However, these conventional batteries have safety issues as they typically contain toxic, flammable, and corrosive materials.[1,2] For large-scale energy storage applications these concerns become especially important as they can pose serious health hazards or cause an environmental disruption. Recently, there has been growing interest in solid-state electrolytes as they can make batteries non-flammable, lower maintenance, and also have a longer shelf life due to unity transference number and a lower self-discharge rate.[1] Such batteries can withstand more demanding loads and continue to operate without the fear of catastrophic failure.[2,3] Solid electrolytes also have the potential to improve battery performance since they have the potential to be utilized with elemental metals such as lithium or sodium for the anode, which would increase the energy density of the battery.[4] For these reasons, all-solid-state batteries are emerging as suitable candidates for large-scale energy storage. Some examples of solid electrolytes include NASICON, chalcogenide glasses, garnets, and LiPON, but their major drawbacks are that their synthesis and processing methods are energy extensive and complex or limited in scale.[5–10]

Recently developed lithium-rich anti-perovskites (LiRAP) with the formula Li_3OX, where X is a halogen or mixture of halogens, was inspired by the F^- superionic conductivity of the $NaMgF_3$ perovskite.[10] Zhao et al. proposed that the electronically inverted anti-perovskite configuration would yield Li^+ superionic conductivity as the Li^+ cation would become the conductive species.[10] Since then, interest in the LiRAP has grown and it has been the subject of many electrochemical experiments and theoretical studies to determine its suitability as a solid electrolyte.[11–17]

Whenever a new lithium compound is discovered, a common trend in the battery community is to investigate the sodium analog.[18] Anti-perovskites are not an exception: shortly after the conductivity of the LiRAP was reported, so was the ionic conductivity of the NaRAP analog.[19] Na-ion batteries are considered a possible lower-cost alternative to Li-ion batteries due to the abundance of sodium in the Earth's crust which is orders of magnitude higher than that of lithium.[20] This positions Na-ion batteries as a candidate for large-scale energy storage systems.[20]

Previous efforts to increase the conductivity of anti-perovskite involved defect engineering such as doping or non-stoichiometric mixtures during synthesis.[11,19] We chose a complementary approach and sought to increase the ionic conductivity in the NaRAP via a suitable post-processing method.

Spark plasma sintering (SPS) is a processing technique which can rapidly densify solid materials compared to conventional sintering or hot-pressing techniques. These techniques employ radiative heating while in SPS, rapid Joule heating takes place. Materials thus can be prepared within minutes with densities in excess of 90% of their theoretical value.[21] Since SPS allows for the intimate joining of materials with disparate melting and sintering temperatures, this technique has been extended to solid-state electrolytes and all solid-state batteries where it has been demonstrated that the mass transport phenomena are enhanced due to the increased inter-particle contact area.[22–26]

In this work, the NaRAP Na_3OBr was synthesized by a single step solid-state reaction. We processed Na_3OBr via room-temperature cold-pressing (CP) and SPS and compared the effects of the two methods on the local microstructure and the electrochemical performance. In addition, we investigated the performance of Na_3OBr by considering the formation energies of intrinsic diffusion mediating defects as estimated from first principles calculations.

Experimental

Material synthesis.—Due to the hygroscopic nature of the starting materials and the electrolyte, all synthesis, material handling, and measurements were carried out in an Argon filled glove box (MBraun, H_2O < 1 ppm, O2 < 1 ppm) unless otherwise noted. Na_3OBr was synthesized from sodium oxide (Sigma Aldrich, 80% Na_2O and 20% Na_2O_2) and NaBr (Alfa Aesar, 99.999%). These precursors were mixed and ground into a fine powder with an agate mortar and pestle for 10 minutes. The mixture was hydraulically pressed into 13 mm-diameter cylindrical pellets at 370 MPa using a stainless steel die (Carver, Inc.). The pellets were placed on an alumina crucible and heated in an electric furnace at 450°C for 24 hours where the solid-state reaction described in Eq. 1. took place.

$$0.8\,Na_2O + 0.2\,Na_2O_2 + NaBr \rightarrow Na_3OBr + 0.1\,O_2 \uparrow \quad [1]$$

Subsequently the pellets were quenched to room temperature by sandwiching the pellets between two large copper blocks. To make the CP sample, the as-synthesized Na_3OBr pellets were ground into a fine powder and pressed at room temperature into a 28 mm diameter pellets with a stainless steel die (Carver, Inc.) at a pressure of 60 MPa. The CP pellet was heated to 450°C for 24 hours and quenched by sandwiching between two copper blocks. To form the SPS sample, as-synthesized Na_3OBr pellets were ground into a fine powder in agate mortar and pestle. The powder was loaded into a 20 mm diameter graphite die with the interior lined with a graphite sheet. The loaded graphite die was placed into the chamber of the SPS machine (Thermal Technology SPS 10–3) and pressed to a preload pressure of 5 MPa. The loaded dies were briefly exposed to air during transport from glove box to SPS equipment. A tight fitting between the graphite

*Electrochemical Society Student Member.
**Electrochemical Society Member.
[z]E-mail: shmeng@ucsd.edu

die and graphite foil provides an adequate seal thus protecting the material from moisture during its brief transport in air. The material was heated to 450°C at a rate of 100°C/min and subjected to a pressure of 60 MPa at a ramp rate of 100 MPa/min. The temperature and applied pressure dwell times were 5 minutes each. The pellet was conductively cooled to room temperature within the SPS chamber. The heat-treatment and pressurization were all conducted in the flowing argon environment.

Upon completion of the respective heat treatment, the surfaces of both the CP and SPS pellets were polished with sandpaper. The dimensions of the pellets were recorded.

Materials characterization.—The relative density of the SPS sample was determined by Archimedes' principle with toluene as the immersing fluid. To ensure that our samples did not react with toluene, a pellet fragment of Na_3OBr was immersed in toluene for 1 hour and then dried at 120°C for 12 hours. The mass of the sample was recorded before immersion and after drying. The relative density of the CP material was calculated by measuring the mass and the dimensions of the pellet. The microstructure of the CP and SPS samples were obtained by imaging their fracture cross sections with a scanning electron microscope (SEM). The as-synthesized Na_3OBr powder was also imaged. Iridium was sputtered onto the SEM samples by an Emitech sputter coater for 7 seconds with a current of 85 mA. Images were obtained with a Philips XL-30 SEM operating at 5 kV. The images were analyzed with ImageJ to quantify the area percentage of void spaces.[27] The sample was briefly exposed to air during transport from the sputtering tool to the SEM, but we do not expect this to drastically change the relative porosity of our samples.

Energy-Dispersive X-ray Spectroscopy (EDS) was conducted on a Philips XL30 ESEM using a 40 μm aperture. Samples were prepared for the SEM as previously described. EDS was conducted on the surface of an as-synthesized pellet. The energy range of the scan was from 0–15 keV as the accelerating beam voltage was 15 kV. The dwell time was 5 minutes.

X-ray diffraction (XRD) samples were prepared in a glove box and sealed using polyimide tape to protect the samples from atmospheric conditions during acquisition. XRD data of the as-synthesized, CP, and SPS samples were collected by a Rigaku Rotaflex RU-200B diffractometer using Cu K_α radiation. The 2θ scan range was from 10 to 70°. Rietveld refinement on the XRD data was carried out using GSAS software with EXPGUI in the range of 25–70°.[28] The lower angle data was excluded since the polyimide tape yields a broad peak from 15–25°.

Electrochemical characterization.—Electrochemical impedance spectroscopy (EIS) measurements were conducted using an impedance analyzer (Solartron 1260). The frequency range was 1 MHz–10 mHz and the applied AC potential was 100 mV. Colloidal silver paste (Ted Pella, 16032) was applied to the top and bottom surfaces of the CP and SPS pellets to serve as electrodes and stainless steel plates were used as the current collectors. The paste was cured at 120°C for 30 min on each side to remove the solvents. Temperature-dependent impedance measurements were collected by heating the pellets in an electric furnace from room temperature to 280°C in 20°C increments. The heating rate was 1°C/min to avoid temperature overshoot and measurements were conducted after the target temperature was held for an hour to allow for temperature stabilization. The ionic conductivity was determined from fitting the Nyquist plots and normalizing via the dimensions of the pellet. The activation energy (E_a) for Na ion diffusion was calculated from the slope of the Arrhenius plot.

Defect modeling and formation energy computation.—All density functional theory (DFT) calculations were performed using the Vienna Ab initio Simulation Package (VASP)[29] within the projector augmented wave approach.[30] The Perdew-Burke-Ernzerhof (PBE) generalized-gradient approximation (GGA) was adopted for all calculations.[31] A *k*-point density of at least 1000/(number of atoms in unit cell) was used and the energy cutoff was set to 520 eV.

A 3 × 3 × 3 supercell with 135 atoms was used to construct the configurations for all types of defects, including a Na Frenkel defect ($V_{Na} + Na_i$), a Na vacancy coupled with substitutional exchange of O by Br ($V_{Na} + Br_O$) and a Na interstitial coupled with substitutional exchange of Br by O ($Na_i + O_{Br}$).

We estimated the mixing energy of structures with defects using the following equation:

$$E_{mix} = E\,(Na_{2-x}O_{1-x}Br_x) - (1-x)\,E\,(Na_2O) - x\,E(NaBr), \qquad [2]$$

where $E\,(Na_{2-x}O_{1-x}Br_x)$ is the total energy of the configuration of interest, x is the fraction of Br and $E\,(Na_2O)$ and $E\,(NaBr)$ are the total energy per formula unit of Na_2O and NaBr, respectively. We also estimated the mixing energy of defect-free Na_3OBr and the result was normalized to a 3 × 3 × 3 supercell for comparison. The total energy of Na_2O, NaBr, and defect-free Na_3OBr were queried from the Materials Project database[32,33] and the analyses were carried out using the Python Materials Genomics (pymatgen) library.[34]

Results and Discussion

To verify the phase purity of our synthesized material, X-ray diffraction data was collected from the as-synthesized, CP, and SPS materials. Figure 1a presents the respective crystalline structures and phases of our materials. Crystal structure information was determined by Rietveld refinement and the atomic positions of each phase are presented in Table I. The main phase present in the sample was found to be cubic Na_3OBr with trace impurities identified as unreacted NaBr (<5 wt%). The space group P m −3 m (221) of the NaRAP crystal structure is represented in Figure 1b. According to Rietveld refinement results, the synthesis pathway described in Eq. 1 resulted in the successful formation of Na_3OBr from readily available sodium oxide sources, which consist of a mixture of sodium oxide and sodium peroxide. Thus we demonstrate an alternative synthesis pathway without the use of sodium metal or NaOH as previously reported.[19,35,38,47] The detailed refinement calculations are shown in Figure 2, and the obtained lattice parameters, tabulated in Table II, are in good agreement with previous reports.[19,35] Subsequent processing of the NaRAP material did not change the crystal structure; in both the CP and SPS cases, the sample was predominantly the NaRAP phase. As seen in Table II, the weight percent of unreacted NaBr is subsequently reduced after the material was processed. There is likely some unreacted sodium oxide which was undetectable with our lab XRD and processing of the as-synthesized material drove the reaction between sodium oxide and NaBr to further completion.

Since the as-synthesized pellets came into contact with copper blocks during the quenching process, EDS was conducted in order to investigate any presence of copper. The spectrum is shown in Figure 1c. Major peaks were identified as the O Kα (0.52 keV), Na Kα (1.04 keV), and Br Lα (1.49 keV) peaks. The Ir M peak (1.98 keV) is from the sputtered Ir and the C Kα peak (0.28 eV) is from the environment or from the instrument. Although the Cu Lα line (0.930 keV) would be difficult to detect as the signal would be masked by the Na Kα peak, we also see no significant signal at 8.04 keV, the characteristic Cu Kα line. Coupled with the X-ray diffraction results, where Na_3OBr and NaBr accounted for the observed peaks, copper is not incorporated into our samples.

To determine a suitable immersion medium for the density measurement by Archimedes' principle, the results of the toluene stability test are shown in Table III. The difference in mass between the pellet before and after immersion is negligible and the pellet fragment remained intact after the test. Based on this result, Na_3OBr is stable in toluene. The relative density of the CP and SPS samples compared to Na_3OBr's theoretical value was measured to be 89% and 96%, respectively. This is the first indication that SPS densified our Na_3OBr sample to a higher degree than CP. To examine the microstructure of Na_3OBr, SEM images of the as-synthesized powder, CP cross section, and SPS cross section were collected. These images are shown

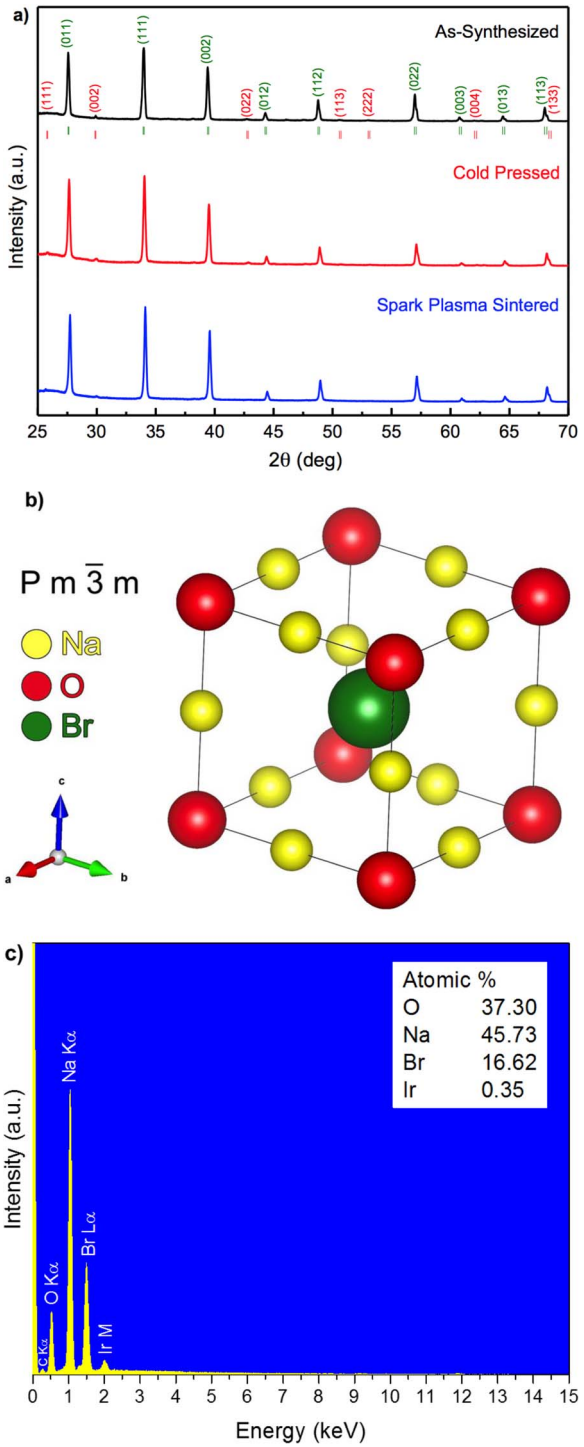

Figure 1. a) XRD pattern of Na_3OBr: as-synthesized (top), Cold-pressed (middle) and SPS (bottom). Green and red Miller indexes correspond to the Na_3OBr phase and NaBr phase, respectively. b) Space group representation of Na_3OBr crystal. c) EDS spectrum taken on the surface fragment of an as-synthesized Na_3OBr sample. Inset: atomic percentages of the detected elements.

in Figures 3a, 3b, and 3c, respectively. The particle morphologies are similar between the as-synthesized, CP and SPS samples, however, in the as-synthesized and CP samples, a significant amount of porosity is evident. This is in contrast to the SPS sample, where there is an observable reduction in the amount of pores. ImageJ was used to quantify the area percentage of the porosity in the CP and SPS samples and the results are shown in Figures 3d and 3e. The area percentage of

Table I. Atomic positions for Na_3OBr and NaBr phase for the as-synthesized, CP, and SPS samples, as determined from Rietveld refinement.

Atoms	X	Y	Z	Occupancy
		Na_3OBr		
Na	1/2	0	0	3
O	0	0	0	1
Br	1/2	1/2	1/2	1
		NaBr		
Na	0	0	0	1
Br	1/2	1/2	1/2	1

the porosity was calculated to be 3.98% for the SPS sample compared to 13.79% for the CP sample. These porosity values complement our density measurements well. Although SPS densified our material, the porosity of the material is still visible in the SEM image, in contrast to sulfide-based materials, where SPS processing resulted in a nearly uniformly dense material.[36] A detailed analysis of the contribution of the porosity to the ionic conductivity is discussed in the following section.

Electrochemical impedance spectroscopy was performed to analyze the Na^+ ionic conductivity of the CP and SPS samples. Figures 4a and 4b show the Nyquist plots of the CP and SPS samples, respectively, measured at 180°C. Our equivalent circuit was derived from a brick-layer model proposed by Huggins.[37] The circuit consists of resistors and constant phase elements (CPE) in the following configuration to represent our cell: The resistor, R_b, represents bulk impedance while the parallel RC combination, R_{int} and CPE_{int}, represents the interfacial impedance contribution. CPE_{geom} represents the presence of the electrolyte material having a finite dielectric constant between two electronically conducting electrodes. These elements model the arc formed from the impedance response. The last element in series, $CPE_{electrode}$, captures the low frequency electric double layer effects of the ion blocking electrode/electrolyte interface, found at the tail section of the spectra. For our CP sample, interfacial impedance was found to have a larger contribution compared to the bulk impedance. A similar result was also observed with the LiRAP, where it was reported that the dominant contribution to the impedance spectra was from the grain boundaries.[38] While different phenomena have been reported to be responsible for resistive behavior in various ionic conductors,[39] the large interfacial impedance in the CP sample specifically can be attributed to the poor sintering and low relative density of the sample. In contrast, the interfacial impedance of the SPS sample was found to be drastically reduced and its conductivity was calculated to be 1.29×10^{-5} S/cm compared to 8.91×10^{-8} S/cm for the CP sample. This is expected as our SEM image shows a reduction in the open porosities of the SPS sample; the increase in contact area between Na_3OBr particles is due to the improved sintering. Although the interfacial impedance of the SPS material is reduced by three orders of magnitude, interestingly, the results for the bulk conductivity are similar between CP and SPS: 2.16×10^{-7} S/cm and 9.02×10^{-7} S/cm, respectively. Thus, this comparison between CP and SPS enabled us to investigate not only the effect of SPS on the sintering and interfacial conductivity, but also the intrinsic bulk ionic conductivity of Na_3OBr. The activation energy barrier was calculated from the linear Arrhenius plot displayed in Figure 4c and determined to be 1.142 eV and 0.837 eV for the CP and SPS samples, respectively. Both the decrease in the Na^+ migration energy barrier and the reduction in the interfacial impedance in the SPS sample are attributed to the improved sintering, which ultimately led to an increased overall ionic conductivity. We also previously observed a higher weight percent of the Na_3OBr phase after processing via SPS, which may have contributed to an increase in the overall conductivity by reducing the concentration of impurities.

Although we observed an improvement in ion conductivity of Na_3OBr processed via SPS, its conductivity is on the order of 10^{-6} S/cm at temperatures greater than 200°C. We can infer that the room

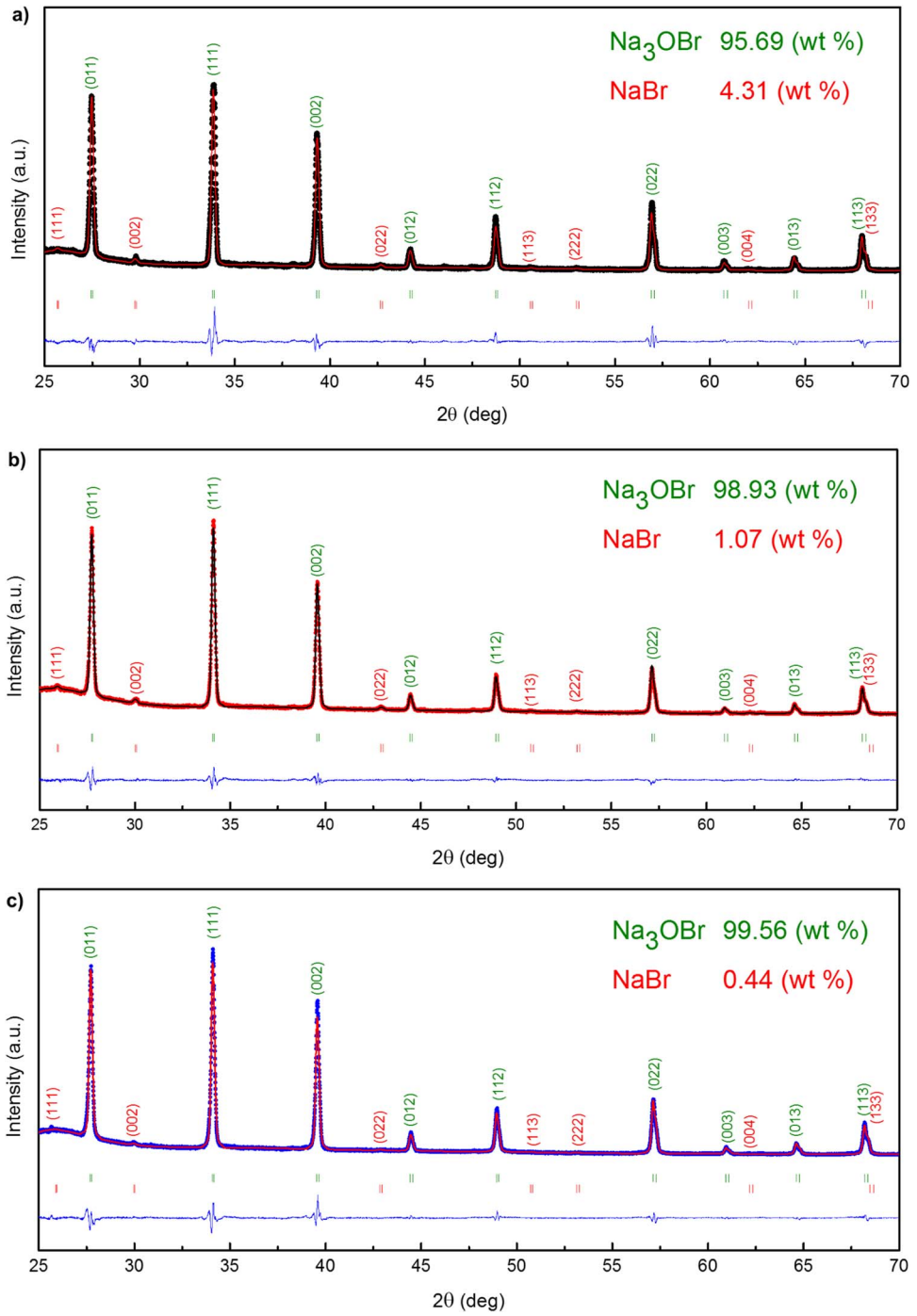

Figure 2. Rietveld refinement of the a) as-synthesized sample, b) CP sample, and c) SPS sample. Green and red miller indexes correspond to the Na_3OBr and NaBr phases, respectively.

Table II. Phase fractions and lattice parameters for the as-synthesized, CP, and SPS samples, as determined from Rietveld refinement.

Phase	As-Synthesized wt%	CP wt%	SPS wt%	As-Synthesized Lattice Parameter (a=b=c)	CP Lattice Parameter (a=b=c)	SPS Lattice Parameter (a=b=c)
Na_3OBr	95.70%	98.93%	99.56%	4.55757(6) Å	4.56418(6) Å	4.56216(5) Å
NaBr	4.31%	1.07%	0.44%	5.96238(6) Å	5.9705(5) Å	5.97430(15) Å

(a) Reliability factors: R_b 6.76%, $R_{wp} = 9.23\%$. (b) Reliability factors: R_b 4.88%, $R_{wp} = 6.52\%$. (c) Reliability factors: R_b 5.48%, $R_{wp} = 7.18\%$.

Table III. Mass of a Na_3OBr pellet fragment before and after immersion in toluene.

Mass before immersion in toluene (g)	Mass after immersion in toluene (g)	Percent difference
0.2185	0.2184	0.046

temperature conductivity of NaRAP would be much lower than LiRAP which has reported conductivities on the order of 10^{-6} S/cm at room temperature.[38] Previous studies have been conducted to explain the mechanism behind lithium superionic conductivity in LiRAP.[13–17,40–43] Ab initio molecular dynamics simulations showed that pristine anti-perovskites are not intrinsically superionic conductors; their dense crystal structures do not provide paths for fast ion diffusion.[44] The ionic conductivity of these materials therefore depends on defect density. In contrast, other Li-ion solid-state conductors such as lithium lanthanum titanate (LLTO) and $Li_{10}GeP_2S_{12}$ (LGPS) contain vacant crystallographic sites which facilitate superior ion migration.[45,46] It has been demonstrated that experimentally introducing vacancies in LiRAPs dramatically increases lithium ion conductivity.[44] Thus, for LiRAP to have superionic conductivity, ion transport-facilitating defects must be deliberately generated during synthesis or processing.[16]

In pristine anti-perovskites, the only defects that can facilitate ion transport are thermally generated. One such defect is an interstitial from a Frenkel defect. In Li_3OCl, the high formation energy of the Li Frenkel defect (1.94 eV) suggests it is extremely difficult to generate a significant concentration of these defects solely by thermal excitation.[17] The computed mixing energies of three types of defects for Na_3OBr are plotted in Figure 5. For the Na Frenkel defect, its mixing energy is 2.53 eV higher compared with defect-free Na_3OBr, which means that the energetic cost of forming the Na Frenkel defect

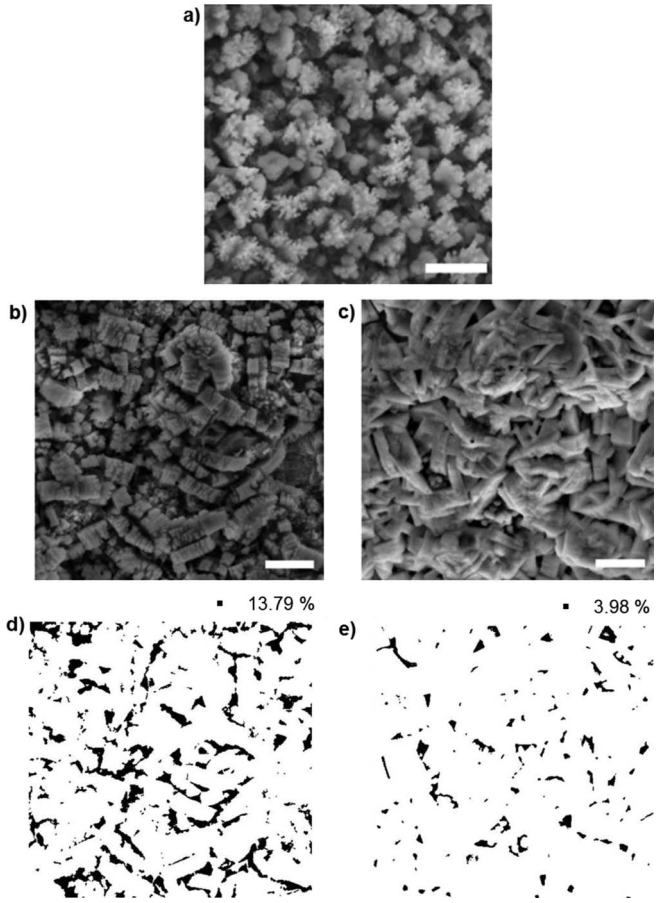

Figure 3. SEM and ImageJ analysis of CP and SPS pellets. SEM images of a) the as-synthesized powder, b) CP cross section, and c) SPS cross section. Scale bars are all 1 μm. ImageJ color analysis and quantification of the void spaces in the d) CP and e) SPS SEM images.

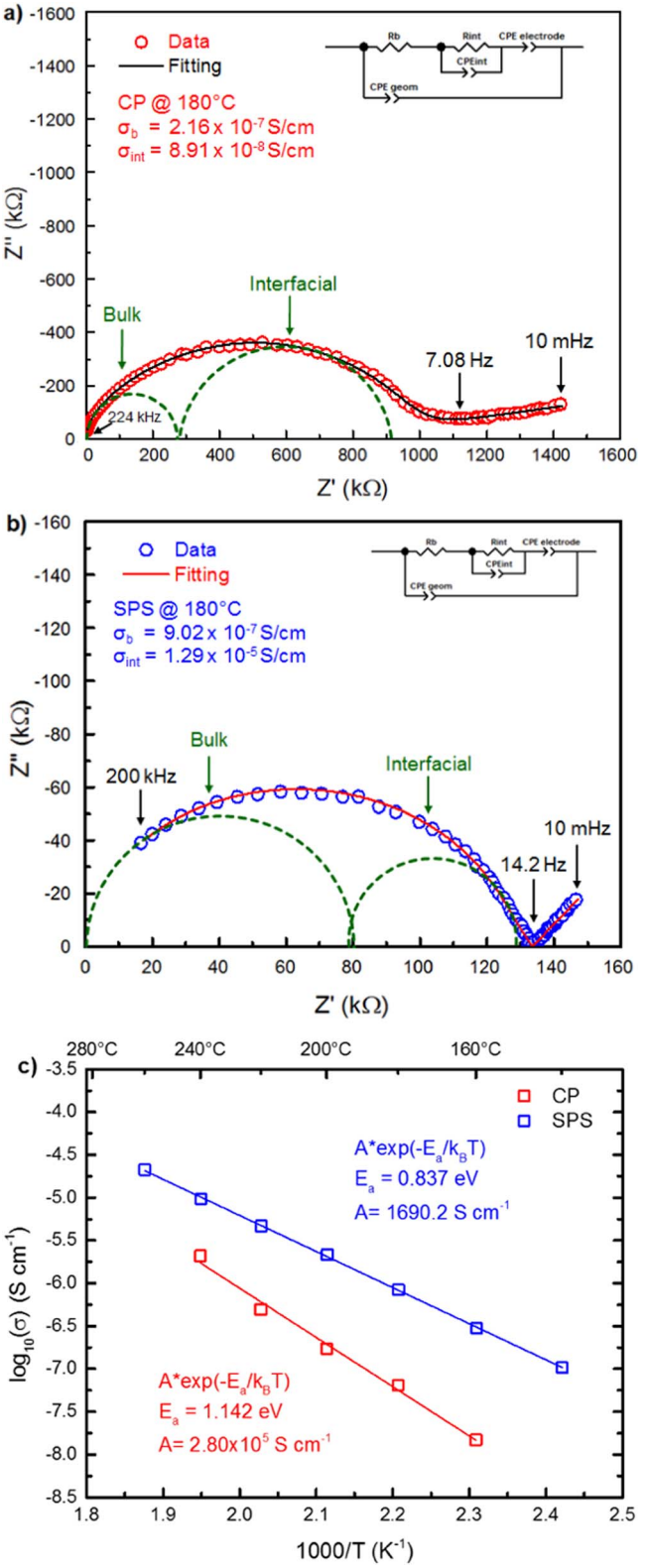

Figure 4. Electrochemical Results. Nyquist plot and fitting of the a) CP sample and b) SPS sample, taken at 180°C. c) Arrhenius plot of the CP and SPS samples.

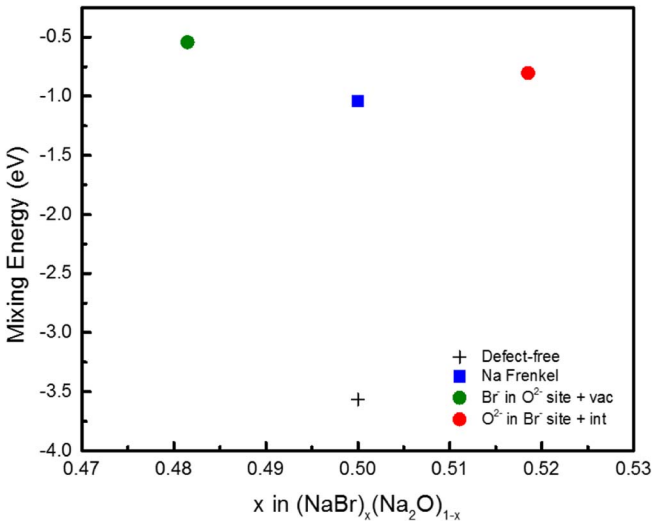

Figure 5. Mixing energies for charge-neutral defects represented as deviations from the ideal Na_3OBr anti-perovskite stoichiometry.

in Na_3OBr is even higher than that in Li_3OCl. We also explored other possible cases for generating a Na vacancy or interstitial, such as Br^- for O^{2-} and O^{2-} for Br^-, respectively, which were previously found to be more energetically favorable than the Frenkel defect in Li_3OCl.[17] In Na_3OBr, the Br^- for O^{2-} substitutional defect had a mixing energy of 2.77 eV and the O^{2-} for Br^- substitution had a mixing energy of 3.03 eV. Unlike Li_3OCl, these energetic costs are all higher than even the Na Frenkel defect.[17]

The mixing energies of the ion diffusion-facilitating defects in Na_3OBr are all much larger than the mixing energies in LiRAPs. This, coupled with the phase purity of our Na_3OBr samples as determined from XRD, could explain the relatively lower overall conductivity of Na_3OBr versus LiRAPs. We can infer that the amount of thermally generated defects in anti-perovskites, whether vacancies or interstitials, is much lower compared to the concentration of defects that can result from doping or depletion during synthesis.[16] In this context, NaRAPs should be engineered in a similar manner to LiRAPs. Namely, a combination of optimization strategies such as SPS, doping using aliovalent halogens, divalent cations, or the creation of non-stoichiometric anti-perovskites by depletion, could yield NaRAPs with higher ionic conductivity.[11,14,15,38,40]

Conclusions

We successfully synthesized the solid electrolyte Na_3OBr via a single step heat-treatment from readily available sources. This synthesis method can also be used to synthesize different NaRAP compounds such as Na_3OCl or $Na_3OCl_xBr_{(1-x)}$ $(0 < x < 1)$. This reaction mechanism can be easily scaled up for production of large quantities of solid-state electrolytes and modified to create NaRAP compounds with various halogens. We also demonstrated that SPS is an effective technique to reduce the interfacial impedance and also the overall activation energy of the solid-state electrolyte. We found the bulk conductivity of Na_3OBr to be on the order of 10^{-7} S/cm at 180°C regardless of the processing technique used. From DFT calculations we conclude that ion diffusion-mediating defects in the material are associated with high formation energies, much higher than in LiRAPs. Future work to increase the ionic conductivity of NaRAP should involve a combination of aliovalent and isovalent substitutions in conjunction with advanced processing such as SPS.

Acknowledgments

This work was supported by the National Science Foundation's Designing Materials to Revolutionize and Engineer our Future (DMREF) program under grant No. 1436976. Some of the computations in this work were performed using the Extreme Science and Engineering Discovery Environment (XSEDE), which is supported by National Science Foundation grant number ACI-1053575. This work was performed in part at the San Diego Nanotechnology Infrastructure (SDNI), a member of the National Nanotechnology Coordinated Infrastructure, which is supported by the National Science Foundation (grant ECCS-1542148).

References

1. X. Kang, *Chem. Rev.*, **104**, 4303 (2004).
2. J. B. Goodenough and Y. Kim, *Chemistry of Materials*, **22**, 587 (2010).
3. N. J. Dudney, *Materials Science and Engineering B*, **116**, 245 (2005).
4. L. Baggetto, R. a H. Niessen, F. Roozehoom, and P. H. L. Notten, *Adv. Funct. Mater.*, **18**, 1057 (2008).
5. C. S. Nimisha, K. Y. Rao, G. Vekatesh, G. M. Rao, and N. Munichandraiah, *Thin Solid Films*, **519**(10), 3401 (2001).
6. V. Thangadurai, D. Pinzaru, S. Narayanan, and A. K. Baral, *J. Phys. Chem. Lett.*, **6**(2), 292 (2015).
7. J. B. Goodenough, H. Y.-P. Hong, and J. A. Kafalas, *Materials Research Bulletin*, **11**(2), 203 (1976).
8. A. Hayashi, T. Ohtomo, F. Mizuno, K. Tadanaga, and M. Tatsumisago, *Electrochem. commun.*, **5**, 701 (2003).
9. T. Thompson, J. Wolfenstine, J. Allen, M. Johannes, A. Huq, N. I. David, and J. Sakamoto, *J. Mater. Chem. A*, **2**, 13431 (2014)
10. Z. Zhu, I.-H. Chu, Z. Deng, and S. P. Ong, *Chem. Mater.*, **27**, 8318 (2015).
11. Y. Zhao and L. L. Daemen, *J. Am. Chem. Soc.*, **134**, 15042 (2012).
12. M. H. Braga, J. a. Ferreira, V. Stockhausen, J. E. Oliveira, and A. El-Azab, *J. Mater. Chem. A*, **2**, 5470 (2014).
13. X. Lü, Gang. Wu, W. J. Howard, A. Chen, Y. Zhao, L. L. Daemen, and Q. Jia, *Chem. Commun.*, **50**, 11520 (2014).
14. J. Zhang, J. Han, J. Zhu, Z. Lin, M. H. Braga, L. L. Daemen, L. Wang, and Y. Zhao, *Inorg. Chem. Commun.*, **48**, 140 (2014).
15. Z. Deng, B. Radhakrishnan, and S. P. Ong, *Chem. Mater.*, **27**, 3749 (2015).
16. R. Mouta, M. a B. Melo, E. M. Diniz, and C. W. A. Paschoal, *Chem. Mater.*, **26**, 7137 (2014).
17. A. Emly, E. Kioupakis, and A. Van der Ven, *Chem. Mater.*, **25**, 4663 (2013).
18. B. Ellis and L. Nazar, *Current Opinion in Solid State Materials Science*, **16**, 168 (2012).
19. Y. Wang, Q. Wang, Z. Liu, Z. Zhou, S. Li, J. Zhu, R. Zou, Y. Wang, J. Lin, and Y. Zhao, *J. Power Sources*, **293**, 735 (2015).
20. P. Moseley and J. Garche, *Electrochemical Energy Storage for Renewable Sources and Grid Balancing*, 1st Edition. Elsevier, (2014).
21. Z. A. Munir, U. Anselmi-Tamburini, and M. Ohyanagi, *J. Mater. Sci.*, **41**, 763 (2006).
22. A. Mei, Q.-H. Jiang, Y.-H. Lin, and C.-W. Nan, *J. Alloys Compd.*, **486**, 871 (2009).
23. J. Langer, M. J. Hoffmann, and O. Guillon, *Acta Mater.*, **57**, 5454 (2009).
24. G. Delaizir, N. Manafi, G. Jouan, P. Rozier, and M. Dollé, *Solid State Ionics*, **207**, 57 (2012).
25. Y. Kobayashi, T. Takeuchi, M. Tabuchi, K. Ado, and H. Kageyama, *J. Power Sources*, **81-82**, 853 (1999).
26. J.-S. Lee, C.-M. Chang, Y. I. Lee, J.-H. Lee, and S.-H. Hong, *Journal of the American Ceramic Society*, **87**(2), 305 (2004).
27. F. Papadopulos, M. Spinelli, S. Valente, L. Foroni, C. Orrico, F. Alviano, and G. Pasquinelli, *Ultrastructural Pathology*, **31**(6), 401 (2007).
28. M. S. Idris and R. A. M. Osman, *Advanced Materials Research.*, **795**, 479 (2013).
29. G. Kresse and J. Furthmüller, *Phys. Rev.*, **B54**, 11169 (1996).
30. P. E. Blöchl, *Phys. Rev. B*, **50**, 17953 (1994).
31. J. Perdew, K. Burke, and M. Ernzerhof, *Phys. Rev. Lett.*, **77**, 3865 (1996).
32. A. Jain, S. P. Ong, G. Hautier, W. Chen, W. D. Richards, S. Dacek, S. Cholia, D. Gunter, D. Skinner, G. Ceder, and K. A. Persson, *Apl Materials.*, **1**(1), 011002 (2013).
33. S. P. Ong, S. Cholia, A. Jain, M. Brafman, D. Gunter, G. Ceder, and K. A. Persson, *Computational Materials Science.*, **97**, 209 (2015).
34. S. P. Ong, W. D. Richards, A. Jain, G. Hautier, M. Kocher, S. Cholia, D. Gunter, V. L. Chevrier, K. A. Persson, and G. Ceder, *Comput. Mater. Sci.*, **68**, 314 (2013).
35. K. Hippler, S. Sitta, P. Vogt, and H. Sabrowsky, *Acta Crystallogr. Sect. C Cryst. Struct. Commun.*, **46**, 736 (1990).
36. I.-H. Chu, H. Nguyen, S. Hy, Y.-C. Lin, Z. Wang, Z. Xu, Z. Deng, Y. S. Meng, and S. P. Ong, *ACS Appl. Mater. Interfaces*, **8**(12), 7843 2016.
37. R. A. Huggins, *Ionics*, **8**, 300 (2002).
38. S. Li, J. Zhu, Y. Wang, J. Howard, X. Lü, Y. Li, R. Kumar, L. Wang, L. Daemen, and Y. Zhao, *Solid State Ionics*, **284**, 14 (2016).
39. J. Luo, *J. Materiomics*, **1**(1), 22 (2015).
40. Z. Lu, C. Chen, M. Z. Baiyee, X. Chen, C. Niu, and F. Ciucci, *Phys. Chem. Chem. Phys.*, **17**, 32547 (2015).
41. D. J. Schroeder, A. A. Hubaud, and J. T. Vaughey, *Mater. Res. Bull.*, **49**, 614 (2014).
42. J. Li, C. Ma, M. Chi, C. Liang, and N. J. Dudney, *Adv. Energy Mater.*, **5** (2015).

43. Z. Shen, M. Johnsson, Z. Zhao, and M. Nygren, *J. Am. Ceram. Soc.*, **85**, 1921 (2002).
44. Y. Zhang, Y. Zhao, and C. Changfeng, *Phys. Rev. B*, **87**, 134303 (2013).
45. N. Kamaya, K. Homma, Y. Yamakawa, M. Hirayama, R. Kanno, M. Yonemura, T. Kamiyama, Y. Kato, S. Hama, K. Kawamoto, and K. Mitsui, *A. Nat. Mater.*, **10**, 682 (2011).
46. D. Qian, B. Xu, H.-M. Cho, T. Hatsukade, K. J. Carroll, and Y. S. Meng, *Chem. Mater.*, **24**(14), 2744 (2012).
47. H. Sabrowsky, K. Paszkowski, D. Reddig, R. Bochum, and D. Bochum, *Zeitschrift für Naturforschung B*, **43**(2), 238 (2015).